Journal of
Materials Chemistry A

PAPER

View Article Online
View Journal | View Issue

Cite this: *J. Mater. Chem. A*, 2025, **13**, 21819

A vanadium-doped Cu_xO nanorod array with modulated electronic structure for enhanced aqueous energy storage†

Jiaxin Luo,[ab] Yang Qin,[a] Meina Tan,[a] Shengtong Lv,[a] Fazhi Zhang,[a] Xuhui Zhao,[a] Yiping Wang,*[ab] Gareth R. Williams[c] and Xiaodong Lei*[ab]

Received 5th March 2025
Accepted 27th May 2025

DOI: 10.1039/d5ta01765c

rsc.li/materials-a

The poor intrinsic electronic conductivity of copper-based oxide materials limits their development for aqueous electrochemical energy storage devices (AEESDs). Herein, we developed a self-supporting vanadium-doped Cu_xO nanorod array AEESD *via in situ* transformation using a template precursor and modification with vanadium. Theoretical and experimental analyses illustrate that partial vanadium isomorphic substitution at copper sites can successfully modulate the electronic and lattice structure of the pristine materials, thereby driving electron transfer and resulting in enhanced electrical conductivity and reaction kinetics for energy storage. An AEESD constructed with a V-Cu_xO nanorod array negative electrode shows desirable electrochemical performance, with a high energy density of 1.26 mWh cm^{-2} at a power density of 8.50 mW cm^{-2} and 0.71 mWh cm^{-2} at 85 mW cm^{-2}. The AEESD can effectively power LED lighting. This work provides novel insights into how modulation of the crystal structure of copper-based oxides can enhance their electrochemical performance.

Introduction

With the development of new green energy technologies, there is an urgent demand for high capacity and stable energy storage devices.[1,2] Aqueous electrochemical energy storage devices (AEESDs) have attracted much attention in recent years owing to their particular advantages of high power density (1–10 kW kg^{-1}), the possibility for long-term operation, and low cost. These render them potential candidates to replace lithium-ion batteries.[3–5] Although some low-cost AEESDs exhibit comparable electrochemical performance to lithium-ion batteries, their lower energy density still limits their practical applications.

To address this, there is a substantial body of work exploring state-of-the-art electrode materials to enhance the energy density of AEESDs.[6] For instance, a covalent organic framework/$Ti_3C_2T_x$ composite system exhibited a desirable specific capacitance of 1298.3 F cm^{-3} at 1 A cm^{-3}, and excellent rate performance.[7] A binder-free copper-molybdenum-sulfide electrode has also been reported with a high specific capacity of 633 mAh g^{-1} at 5 mV s^{-1}.[8] Thus, utilizing battery-type electrode materials is a promising method to improve the energy storage capacity of AEESDs. Various battery-type anode materials can be fabricated, including ferric-based,[4,9] vanadium-based,[10] and molybdenum-based materials,[11,12] but copper-based materials have particular potential owing to their multi-valence, low-cost, and high storage capacity. However, low intrinsic electrical conductivity is a major challenge, resulting in poor practical performance.

Recently, several strategies have been devised to improve the electrical conductivity of Cu-based materials. In our previous work, we reported S-anion modified Cu/Cu_2O electrode materials, in which S can affect the electronic structure and provide enhanced electrical conductivity.[13] Other literature reports have found that doping with exogenous cations can result in lattice distortion, thereby modulating the electronic structure of the pristine materials and endowing them with new properties.[14–17] For example, an ethylene molecule-intercalated Co-doped sulfur-deficient MoS_2 formulation for K-ion storage has been reported,[18] in which the Co dopants occupy Mo sites, effecting charge transfer and activating the 1T basal plane.

Vanadium is abundant in nature and has a range of accessible oxidation states. Thus, it is a promising dopant which can be used to adjust the electronic structure of a host material. For instance, it has been reported that a V doped $Ni_{0.2}Mo_{0.8}N$ electrode material exhibits strong electron transfer from V to Ni/Mo/N,[19] and a $Mo_{0.88}V_{0.12}O_{2.94}$ nanostructured electrode shows exceptionally high conductivity and fast ionic diffusion due to the presence of V.[20]

---

[a] *State Key Laboratory of Chemical Resource Engineering, Beijing University of Chemical Technology, Beijing 100029, China*

[b] *Quzhou Institute for Innovation in Resource Chemical Engineering, Zhejiang, 324000, China*

[c] *UCL School of Pharmacy, University College London, 29-39 Brunswick Square, London, WC1N 1AX, UK*

† Electronic supplementary information (ESI) available. See DOI: **https://doi.org/10.1039/d5ta01765c**

Preparing self-supporting electrode materials is another way to improve electrical conductivity. This is achieved by decreasing the contact resistance between active materials and substrates, without using extra binder.[21,22] To this end, in this work we aimed to construct a self-supporting V-doped Cu_xO (V-Cu_xO) nanorod array as a negative electrode for AEESDs. This was undertaken using a simple preparation method, and the electronic structure of the materials was examined using X-ray photoelectron spectroscopy (XPS) and UV-vis diffuse reflectance spectroscopy (UV-vis DRS), together with density of states (DOS) and charge density difference distribution calculations. A porous structure was obtained *via* the *in situ* chemical oxidation process used for synthesis, as revealed by scanning and transmission electron microcopies (SEM and TEM) and pore size distribution measurements. Oxygen vacancies were simultaneously introduced by $NaBH_4$ treatment, as illustrated by XPS and electron paramagnetic resonance (EPR) spectroscopy. As a result of these properties, the V-Cu_xO nanorod array generated in this work presents enhanced electrochemical performance, and potential for high-performance AEESD applications.

Experimental section

Additional experimental details can be found in the ESI.†

Synthesis of $Cu(OH)_2$ precursor samples

Copper hydroxide nanorod assays were obtained by chemical oxidation. First, a 3 × 4 cm^2 copper foam (CF) was washed with ethanol and then with dilute hydrochloric acid under ultrasonication for 10 min each. It was then washed with a large volume of deionized (DI) water and dispersed in DI water for further use. Subsequently, 2.5 M NaOH and 0.1 M $(NH_4)_2S_2O_8$ were dissolved in DI water and ultrasonically mixed at room temperature for 3 min, before the cleaned CF was immersed into this solution. After 20 min, the blue-colored product was taken out, and washed several times with DI water and ethanol. Finally, the $Cu(OH)_2$ precursor was obtained by drying at 60 °C for 6 h.

Synthesis of V-Cu_xO and Cu_xO nanorod arrays

0.06 mmol of NH_4VO_3 was dissolved into 40 mL of DI water under stirring for 10 min at 90 °C. Then, 1 mmol of $NaBH_4$ was added into the resultant light-yellow solution and the mixture sonicated for 2 min. Next, it was transferred into a Teflon-lined autoclave, and the 3 × 2 cm^2 $Cu(OH)_2$ nanorod array was also immersed into this solution. The autoclave was heated to 130 °C and then maintained at this temperature for 4 h. After cooling down to room temperature, the $V_{0.06}$-Cu_xO nanorod array was repeatedly rinsed with deionized water, followed by ethanol, and then dried at 60 °C for 5 h. Samples with different vanadium dopant concentrations were prepared in an analogous manner but with different feedstock amounts of NH_4VO_3 (0, 0.02, 0.04, 0.08, 0.1, 0.2 and 0.5 mmol). The samples obtained were named Cu_xO, $V_{0.02}$-Cu_xO, $V_{0.04}$-Cu_xO, $V_{0.08}$-Cu_xO, $V_{0.1}$-Cu_xO, $V_{0.2}$-Cu_xO and $V_{0.5}$-Cu_xO, respectively. $V_{0.06}$-Cu_xO was selected as the representative sample for detailed characterization, and is hereafter denoted as V-Cu_xO. The mass loadings of V-Cu_xO and Cu_xO on the CF were found to respectively be 12.8 and 20.08 mg cm^{-2}.

Electrochemical performance tests

All electrochemical measurements were carried out with a CHI660E workstation (Chenhua, China). A three-electrode system using 1 M KOH electrolyte and consisting of a Hg/HgO reference electrode, a platinum counter electrode and 1 × 1 cm^2 of the test samples as the working electrode was employed. We performed cyclic voltammetry (CV), galvanostatic charge–discharge (GCD) and electrochemical impedance spectroscopy (EIS) measurements to evaluate the electrochemical performance of the prepared electrode materials. The EIS results were fitted with ZView software. The areal capacity from GCD curves was calculated using the formula: C_s (mAh cm^{-2}) $= (I \times \Delta t)/(A \times 3600)$, where I (mA) is the current, Δt (s) is the discharge time, and A (cm^2) is the contact area of the electrode material with the electrolyte.

Fabrication of aqueous energy storage devices

A 2025-type coin cell device was prepared using a Ni–Cu hydroxide/$Cu(OH)_2$/CF positive electrode as reported in our previous work,[23] a GF/D glass fiber separator, and the as-prepared V-Cu_xO negative electrodes with 1 M KOH as the electrolyte. The energy density (mWh cm^{-2}) and power density (mW cm^{-2}) of the device were calculated using the following equations: $E_s = (I \times \Delta t \times \Delta U)/(2 \times 3600)$ and $P_s = (3600 \times E_s)/\Delta t$, where I (mA cm^{-2}) is the current density, Δt (s) is the discharge time, and ΔU (V) is the potential window of the devices, respectively.

Results and discussion

Morphologies and structures

The two-step process for preparing self-supporting V-Cu_xO and Cu_xO nanorod arrays is depicted in Scheme 1. First, a $Cu(OH)_2$ precursor coating was formed on a CF substrate through a simple chemical oxidation method, which provides sufficient reaction sites for further treatment. After hydrothermal treatment with or without NH_4VO_3, V-Cu_xO and Cu_xO nanorod arrays were densely coated on the CF substrate. This method is low-cost and quick and has low energy-consumption.

Clear color changes can be observed during the material production steps (see Fig. S1 and S2, ESI†). The thickness of Cu_xO and V-Cu_xO coatings on copper foam was determined to be ∼6.9 and ∼17.6 μm through the cross-sectional SEM images shown in Fig. S2d and e,† indicating that the V-Cu_xO coating on copper foam is thicker than Cu_xO, which is conducive to exposing much more active sites for redox reactions. The chemical equations involved in the preparation are provided below:

$$Cu + 4NaOH + (NH_4)_2S_2O_8 \rightarrow Cu(OH)_2 + 2Na_2SO_4 + 2NH_3 + 2H_2O \quad (1)$$

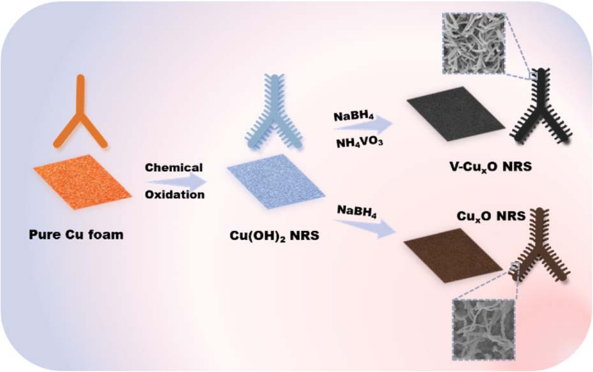

Scheme 1 The synthesis procedure for Cu$_x$O and V-Cu$_x$O nanorod arrays.

$$Cu(OH)_2 + NaBH_4 \rightarrow Cu_2O + CuO + H_2O \quad (2)$$

$$VO_3^- + NaBH_4 \rightarrow V^{4+}(OH) \quad (3)$$

$$Cu(OH)_2 + NaBH_4 + V^{4+} \rightarrow V\text{-}Cu_2O/CuO\ (V\text{-}Cu_xO) \quad (4)$$

$$NaBH_4 + 2H_2O \rightarrow 4H_2 + NaBO_2 \quad (5)$$

The effect of the vanadium feedstock concentration on the morphology of the reaction products was explored (Fig. S3†). It was observed that the nanorod surface became rougher with an increase in the amount of NH_4VO_3 in the feedstock. Based on the SEM images and subsequent XRD analysis, $V_{0.06}$-Cu$_x$O (termed V-Cu$_x$O) was selected for further characterization in this work. Compared with the precursor $Cu(OH)_2$, the V-Cu$_x$O and Cu$_x$O nanorod arrays are rough and porous due to the presence of nanoparticles on the rod surface, as observed in Fig. 1a–c. The nanoparticles in V-Cu$_x$O are smaller than those in Cu$_x$O, indicating that NH_4VO_3 can be utilized as a size modifier. This is likely due to the strong reduction reaction induced by $NaBH_4$, and the subsequent nucleation kinetics.

TEM images (Fig. 1d–f) exhibit that there are many pores in the V-Cu$_x$O and Cu$_x$O samples, which can expose much more active sites for redox reactions and should be conducive to the penetration of electrolyte. As shown in Fig. 1g–j, there are lattice fringes visible in high-resolution TEM (HRTEM) at 0.247, 0.213, 0.232, 0.252 and 0.187 nm. These correspond to the (111) and (200) planes of Cu_2O and the (111), (11−1) and (20−2) planes for the CuO phase in V-Cu$_x$O and Cu$_x$O. This is in agreement with the Selected Area Electron Diffraction (SAED) results (Fig. 1k). However, distinct lattice disturbance can be observed in V-Cu$_x$O, as shown in the inset of Fig. 1j, indicating that introducing vanadium can result in lattice defects. Based on the Energy Dispersive Spectrometer (EDS) line scan and element mapping results (Fig. 1l–p), the distribution of Cu, O and V elements is uniform, indicating that V-Cu$_x$O nanorod arrays were successfully prepared. In addition, the vanadium content was determined by HRTEM-EDS (Fig. S4†), SEM-EDS (Fig. S5†) and Inductively Coupled Plasma-Optical Emission Spectrometry (ICP-OES) (Table S1†) measurements. For comparison, the element mapping and HRTEM-EDS results of the precursor $Cu(OH)_2$ and Cu$_x$O samples are also provided in Fig. S6 and 7.† The vanadium molar ratio in V-Cu$_x$O is about 1.08%. This suggests that vanadium could isomorphously substitute copper sites in the final material. To prove this, further characterization was conducted.

The XPS survey spectrum (Fig. S8a†) and corresponding elemental content (Table S2†) demonstrate that the atomic ratio of V is 1.71%, with the V : Cu ratio of 1 : 10 being consistent with the previous results. As shown in the Cu 2p spectra (Fig. 2a), the peaks of $Cu(OH)_2$ located at 934.45 and 954.20 eV correspond to Cu $2p_{3/2}$ and Cu $2p_{1/2}$ of Cu^{2+}. Therefore, the peaks in V-Cu$_x$O located at 932.32 and 952.07 eV belong to Cu $2p_{3/2}$ and Cu $2p_{1/2}$ of Cu^+/Cu^0, while those at 934.11 and 953.86 eV belong to Cu $2p_{3/2}$ and Cu $2p_{1/2}$ of Cu^{2+}. The corresponding peaks in Cu$_x$O are located at 932.50, 952.25, 934.39 and 954.41 eV.[13] The peak positions shift to lower binding energy by about 0.2 eV in V-Cu$_x$O compared with Cu$_x$O, indicating that the chemical environment of copper sites is affected by the vanadium dopant transferring electrons to copper sites. A similar shift can also be observed in the Cu LMM Auger electron spectra in Fig. S8b.† Peaks in the V-Cu$_x$O V 2p spectrum (Fig. 2b) appear at 516.25 and 523.75 eV, which correspond to V^{4+}.[24–26] The ionic radius of V^{4+} (0.72 Å) is close to that of Cu^+ (0.77 Å) and Cu^{2+} (0.73 Å), indicating that V^{4+} can isomorphously substitute copper sites.

The O 1s spectra (Fig. 2c) of V-Cu$_x$O and Cu$_x$O can be fitted with three peaks ascribed to lattice oxygen ($O_{lattice}$), adsorbed oxygen (O_{ads}) and surface water molecules (OH^-), respectively. A clear peak shift can be observed for $O_{lattice}$, ascribed to V doping changing the chemical environment of the oxygen sites. The ratio between O_{ads} and $O_{lattice}$ can be utilized to evaluate the existence of oxygen vacancies in the lattice (Table S3†).[27] The ratio is found to be higher in V-Cu$_x$O, indicative of O vacancies.

EPR measurements, displayed in Fig. 2d, were also conducted to explore the characteristic oxygen signals of V-Cu$_x$O and Cu$_x$O samples. A free electron factor (g) at about 2.003 indicates that oxygen vacancies are introduced into the crystal lattice during hydrothermal treatment with $NaBH_4$.[28,29] This is desirable, since the literature shows that oxygen vacancies promote charge transfer, leading to higher electronic and ionic conductivity.[30,31]

As shown in Fig. 2e, the three most intense reflections in the XRD pattern arise from the copper foam substrate. The peaks in the $Cu(OH)_2$ pattern match well with the standard PDF card (PDF#13-0420), confirming the formation of the desired phase. However, no reflections from $Cu(OH)_2$ are present in the data for V-Cu$_x$O and Cu$_x$O: only CuO (PDF#48-1548) and Cu_2O (PDF#78-2076) can be seen, indicating the conversion of $Cu(OH)_2$ to CuO and Cu_2O after the hydrothermal reaction. Moreover, no additional peaks are detected after introducing V, implying that no new phase is generated and vanadium does not change the crystal structure of the material.

In comparison with Cu$_x$O, the (111) reflection in V-Cu$_x$O slightly shifts to a higher angle (Fig. S9†), indicating that vanadium incorporation can decrease the lattice parameters due to the smaller ionic radius of V^{4+} (0.72 Å) compared to Cu^+ (0.77 Å) and Cu^{2+} (0.73 Å). The (111) peak position of samples prepared with different vanadium amounts shows a clear trend

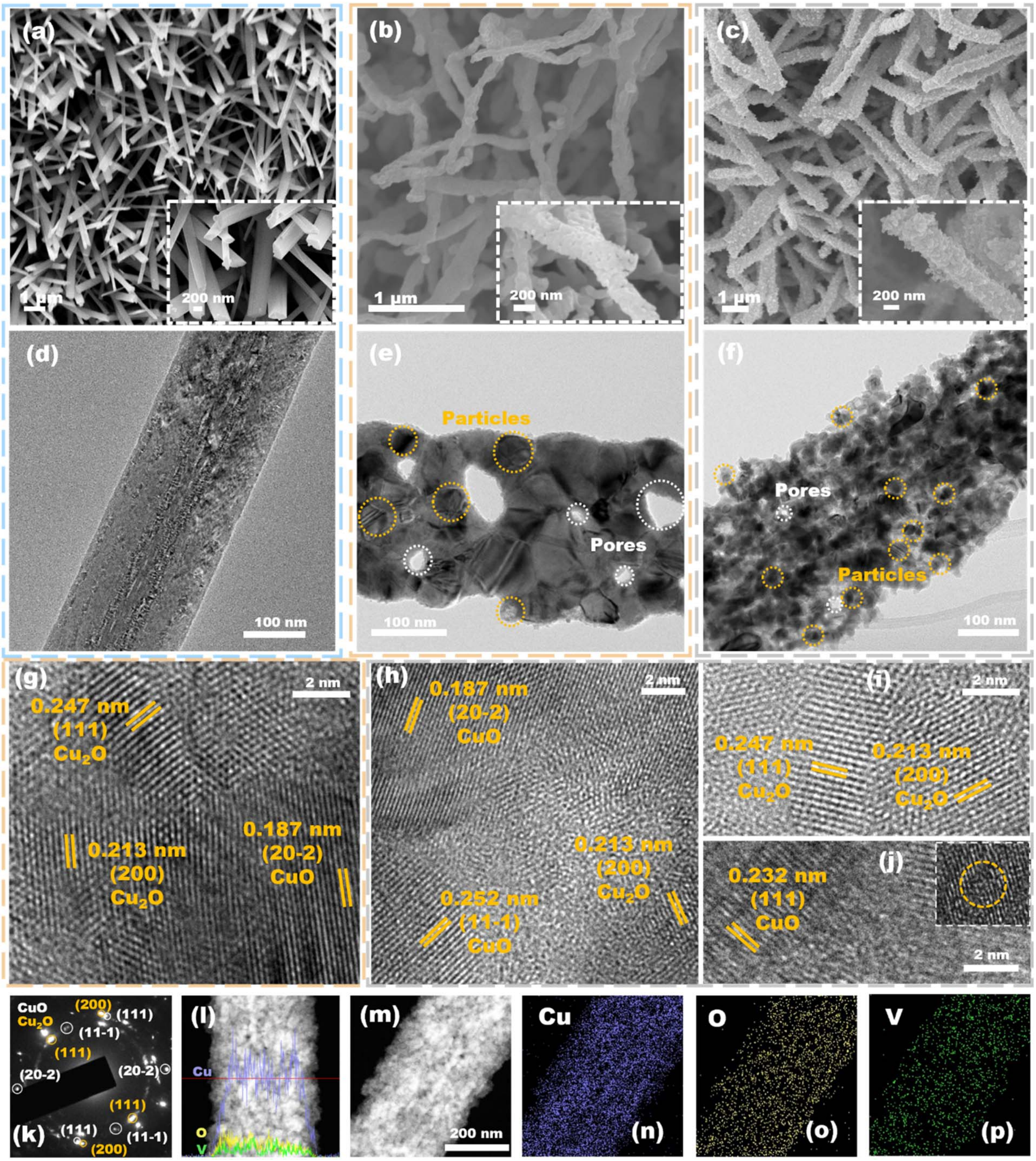

Fig. 1 SEM (a–c) images with enlarged insets, and TEM (d–f) images of the Cu(OH)$_2$, Cu$_x$O and V-Cu$_x$O nanorod arrays, respectively. HRTEM images of Cu$_x$O (g) and V-Cu$_x$O (h–j). An SAED pattern (k), EDS line scan image (l), HAADF-STEM image and element mapping (m–p) of V-Cu$_x$O are also shown.

(Fig. 2e), with the reflection shifting to increasingly higher angles upon the addition of more V and then shifting back to lower angles, indicating that at higher feedstock concentrations vanadium is less likely to substitute copper sites in the lattice. The XRD patterns of the samples with different vanadium amounts are exhibited in Fig. S10.† Given that the largest (111) shift is seen with 0.06 mmol of V in the feedstock, this sample (termed V-Cu$_x$O) was used for further characterization.

Raman spectra (Fig. 2f) of V-Cu$_x$O and Cu$_x$O show characteristic peaks belonging to CuO and Cu$_2$O. The peaks in V-Cu$_x$O exhibit a greater Raman shift, indicating that the lattice parameter decreases after doping, in agreement with XRD. In addition, the Raman spectrum changes dramatically upon doping: some peaks vanish, while three peaks appear at 695–910 cm^{-1}. The latter can be assigned to vibrations of V–O and Cu–O–V bonds, rather than VO$_2$,[32–37] further indicating that

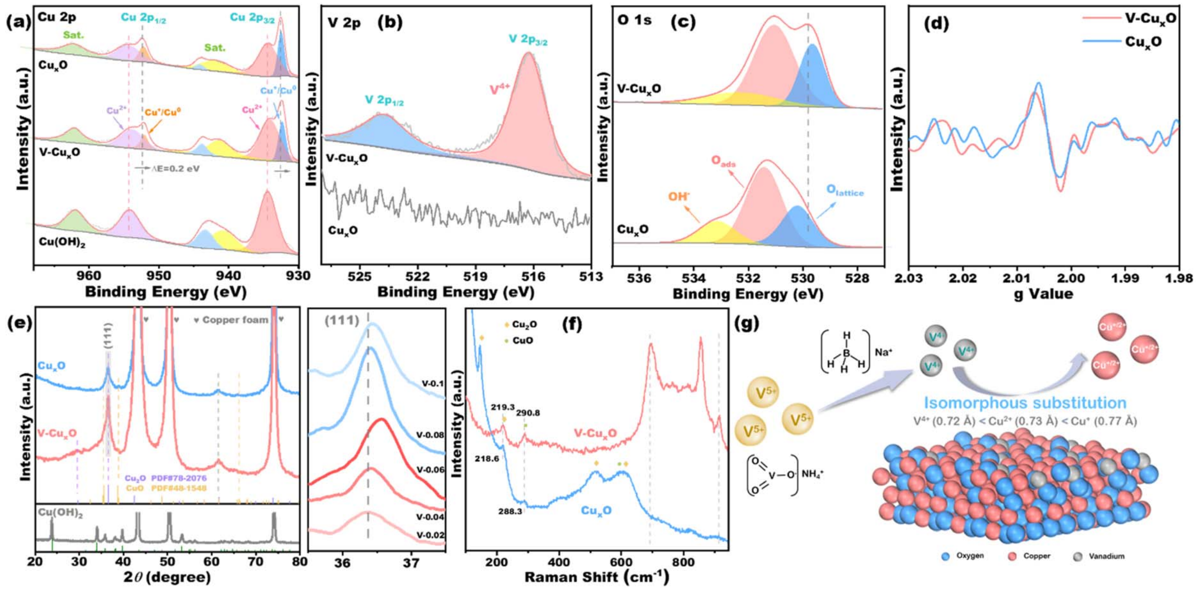

Fig. 2 Cu 2p (a), V 2p (b) and O 1s (c) XPS spectra of V-Cu_xO and Cu_xO. EPR spectra (d) of V-Cu_xO and Cu_xO. (e) XRD patterns of the as-prepared Cu_xO and V-Cu_xO nanorod arrays, and an enlarged view of the (111) reflections in the XRD patterns of samples prepared with different feedstock contents of NH_4VO_3. (f) Raman spectra of the Cu_xO and V-Cu_xO nanorod arrays. A schematic illustration (g) of V^{4+} in the structure of V-Cu_xO.

vanadium was successfully incorporated into the matrix through isomorphous substitution as depicted in Fig. 2g.

Two additional samples with ultra-high vanadium feedstock concentrations were prepared, and denoted as $V_{0.2}$-Cu_xO and $V_{0.5}$-Cu_xO. The corresponding Raman spectra are exhibited in Fig. S11a,† where the lattice parameters of $V_{0.2}$-Cu_xO and $V_{0.5}$-Cu_xO are seen not to decrease, and several weak peaks located at 695–910 cm^{-1} can be seen. The peaks belonging to CuO, Cu_2O and V_2O_5 were clearly observed,[36,38] indicating that the addition of more NH_4VO_3 leads to the formation of a separate V_2O_5 phase due to the insufficient reducing capacity of $NaBH_4$. Thus, at higher feedstock concentrations vanadium is less likely to substitute copper sites in the lattice, and tends to form a new phase (V_2O_5). Furthermore, the SEM images (Fig. S11b and c†) of $V_{0.2}$-Cu_xO and $V_{0.5}$-Cu_xO exhibit agglomerated plate-like morphology with large size, clearly showing that the systems could not maintain a nanorod morphology.

V-Cu_xO and Cu_xO structural models were developed using Materials Studio software, as shown in Fig. 3a. These models provide good fits to the XRD patterns (see Fig. S12†). Measuring the Cu–Cu and Cu–O bond lengths in the V-Cu_xO and Cu_xO models (Fig. 3b) reveals that the average bond lengths in V-Cu_xO are slightly shorter than those in the Cu_xO model (Fig. 3c), confirming that vanadium substitution decreases the bond lengths. Density functional theory (DFT) calculations were carried out to reveal the effect of vanadium doping on the electronic structure. Fig. 3d displays the charge density difference of Cu_xO and V-Cu_xO, indicating that there is a stronger electronic interaction when V is doped into the structure. 2D-slice plots (Fig. 3e) show that charge accumulation on Cu ions adjacent to V increases, which is induced by charge transfer from V to Cu. This is consistent with the XPS results.

The calculated density of states (DOS) in Fig. 3f shows that the d-band center (ε_d) of V-Cu_xO is closer to the Fermi level (E_f) than that of Cu_xO, indicating that vanadium doping can promote charge transfer and therefore should enhance the electrical conductivity. The introduction of vanadium also extends the absorption of electromagnetic radiation to higher wavelengths, as a result of vanadium incorporation into the lattice, as shown in the UV-vis DRS spectra (Fig. 3g).[39] Fig. 3h shows the fitted Tauc-plots of V-Cu_xO and Cu_xO, and the band gap (E_g) values are determined to be approximately 1.38 and 1.78 eV respectively. The narrowed band gap indicates enhanced conductivity of V-Cu_xO. The conductivity values of the bulk samples, displayed in Table S4,† confirm the higher conductivity of V-Cu_xO. Thus, it is clear that doping vanadium can dramatically enhance electrical conductivity and reduce electron transfer resistance.

The OH^- adsorption energies on the surface of V-Cu_xO and Cu_xO were calculated, as shown in Fig. 3i. The OH^- adsorption energy for V-Cu_xO (−0.34 eV) is lower than that for Cu_xO (−0.28 eV), indicating that V-Cu_xO features enhanced adsorption ability for OH^- (see Fig. S13a†). The Mulliken charge analysis provided in Table S5† shows that the total charge-transfer quantities for Cu_xO and V-Cu_xO are respectively −0.05 and −0.04 e, indicating that V-Cu_xO obtains electrons from the electrolyte more quickly.[40] The wettability of V-Cu_xO is greater than that of $Cu(OH)_2$ and Cu_xO, as verified by contact angle tests with KOH electrolyte (Fig. 3j), further confirming that the presence of vanadium can facilitate contact between the electrode and electrolyte. Moreover, by further measuring the pore size distribution (Fig. 3k), it was found that the V-Cu_xO has more micro-pores and meso-pores than Cu_xO. This is in agreement with the earlier observations from SEM and HRTEM,

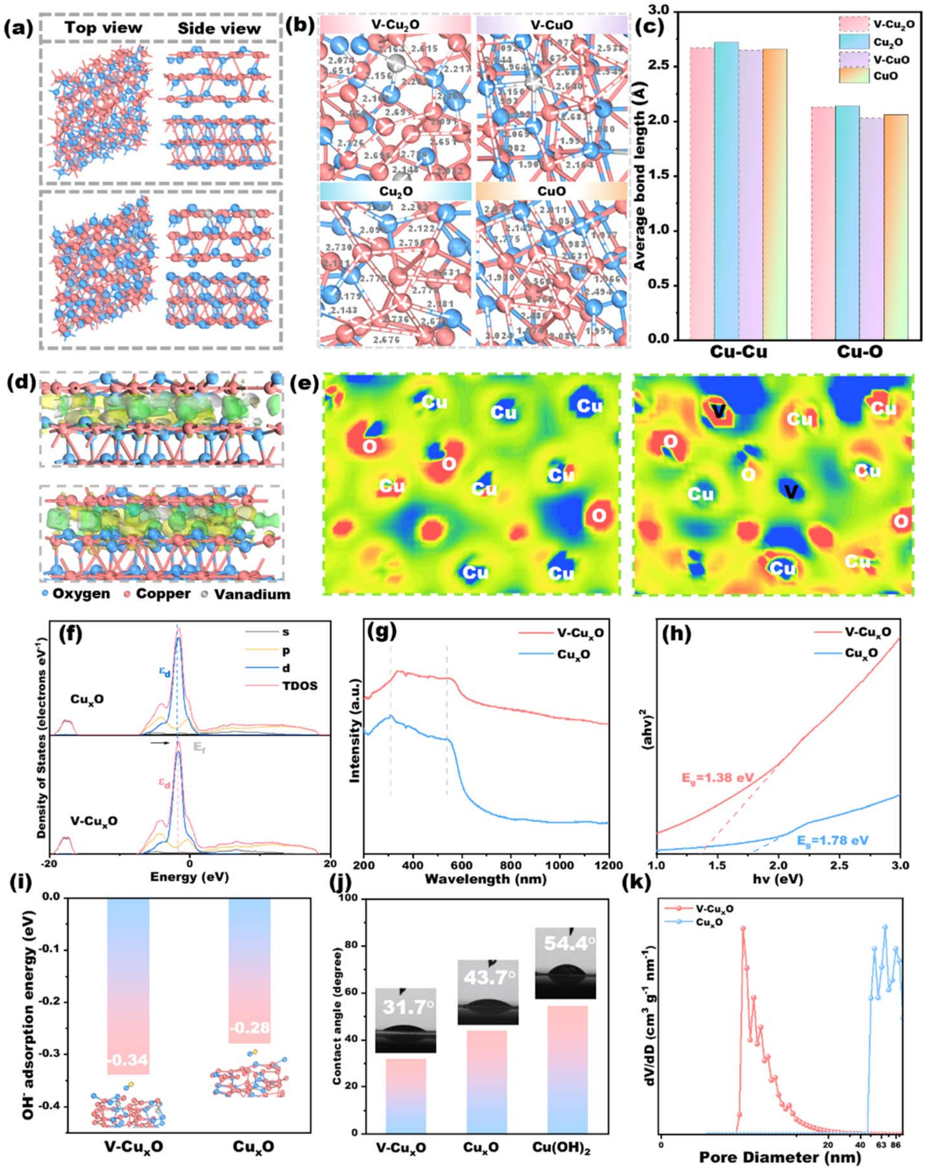

Fig. 3 (a) Optimized models of the Cu_xO and V-Cu_xO structures, and (b) a partial view showing the measured bond lengths. (c) The average Cu–Cu and Cu–O bond lengths. (d) Charge density difference distribution of Cu_xO (top) and V-Cu_xO (bottom); the green and yellow regions denote electronic depletion and accumulation, respectively. (e) The corresponding 2D slice plots of Cu_xO (left) and V-Cu_xO (right); red and blue represent the charge accumulation and depletion regions, respectively. (f) The calculated density of states (DOS) of Cu_xO and V-Cu_xO. (g) UV-vis DRS spectra and (h) the corresponding Tauc-plots. (i) OH^- adsorption energies of Cu_xO and V-Cu_xO. (j) Water contact angles of $Cu(OH)_2$, Cu_xO and V-Cu_xO when exposed to KOH solution. (k) The pore size distributions of Cu_xO and V-Cu_xO, obtained from N_2 adsorption–desorption isotherms.

and should lead to fast penetration and diffusion of the electrolyte. Furthermore, by fitting the plots of current density *vs.* scan rate in CV curves of V-Cu_xO and Cu_xO, the electrochemical active surface area can be determined in terms of the gradient of the line, as shown in Fig. S13b.† The slope of V-Cu_xO is larger than that of Cu_xO, indicating that V-Cu_xO can provide more electrochemically active sites for redox reactions between the electrolyte and electrode than Cu_xO, leading to improved electrochemical performance.

Based on the above experimental and theoretical results, there appear to be a number of structural features in V-Cu_xO which should contribute to potent electrochemical performance. A schematic is presented in Fig. S13c.† First, porous V-Cu_xO possesses numerous micro- and meso-pores, which will permit the fast diffusion and penetration of electrolyte, providing more electrochemically active sites and triggering redox reactions which can occur easily at the surface of the electrode. Secondly, V isomorphously substitutes a portion of the copper sites, affecting the chemical environment of adjacent copper and oxygen sites. Electron density is transferred from vanadium, facilitating the adsorption of electrolyte, and accelerating charge transfer during charge/discharge processes.

Finally, V can narrow the band-gap, lead to the formation of oxygen vacancies and thus improve the ionic and electronic conductivity, leading to fast charge transfer.

Electrochemical properties

To investigate the electrochemical performance of the electrode materials, CV, GCD and EIS tests were performed in 1 M aqueous KOH. Fig. 4a presents the CV curves of the V-Cu_xO electrode at various scan rates from 170 to 30 mV s^{-1} within a potential range of −1.0–0 V *vs.* Hg/HgO. All the curves maintain a similar shape, in which the regular and paired redox peaks indicate battery-like energy storage behavior. In comparison with Cu_xO, the CV curve of V-Cu_xO shows a larger area at a scan rate of 30 mV s^{-1} as shown in Fig. 4b. The corresponding CV curves of Cu_xO at various scan rates are provided in Fig. S14a.† When the current densities of the oxidation and reduction peaks are plotted against the square root of the scan rates (Fig. 4c), V-Cu_xO exhibits markedly sharper gradients. This enhancement is primarily attributed to vanadium doping

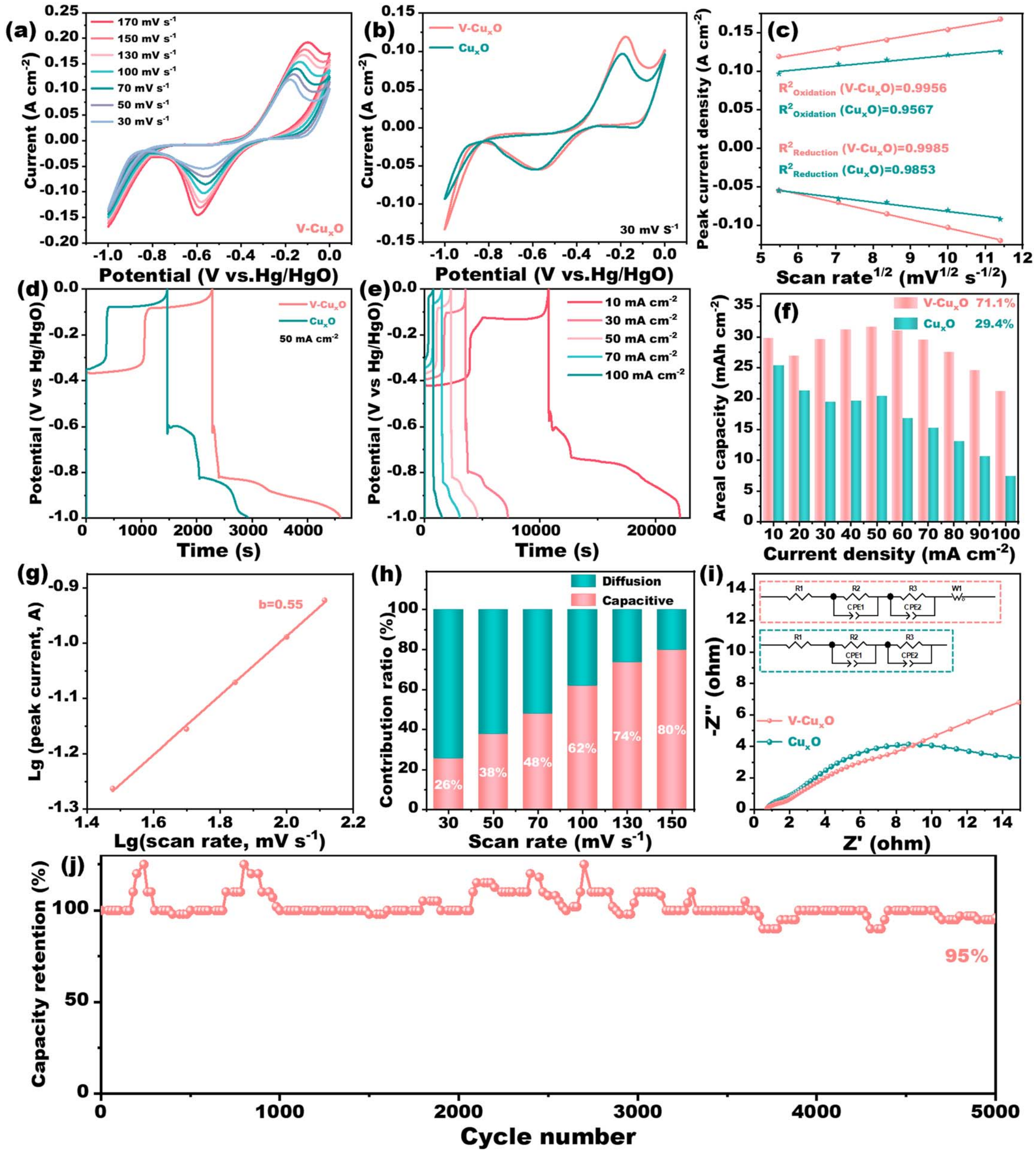

Fig. 4 (a) CV curves of V-Cu_xO at different scan rates. (b) Comparison of the CV data for V-Cu_xO and Cu_xO at 30 mV s^{-1}. (c) Linear fits of the oxidation–reduction peak current densities (i) *versus* the square root of the scanning rate (v). (d) GCD curves of V-Cu_xO and Cu_xO at a current density of 50 mA cm^{-2}. (e) GCD curves of V-Cu_xO at different current densities. (f) The rate capability of V-Cu_xO and Cu_xO at different current densities from 10 to 100 mA cm^{-2}. (g) The linear relationship between lg(i) and lg(v) from the CV curves. (h) The percentage capacitance contributions of the V-Cu_xO electrode at different scan rates from 30 to 150 mV s^{-1}. (i) EIS of the V-Cu_xO and Cu_xO electrodes with different equivalent circuits. (j) The cycling performance of V-Cu_xO at a current density of 150 mA cm^{-2}.

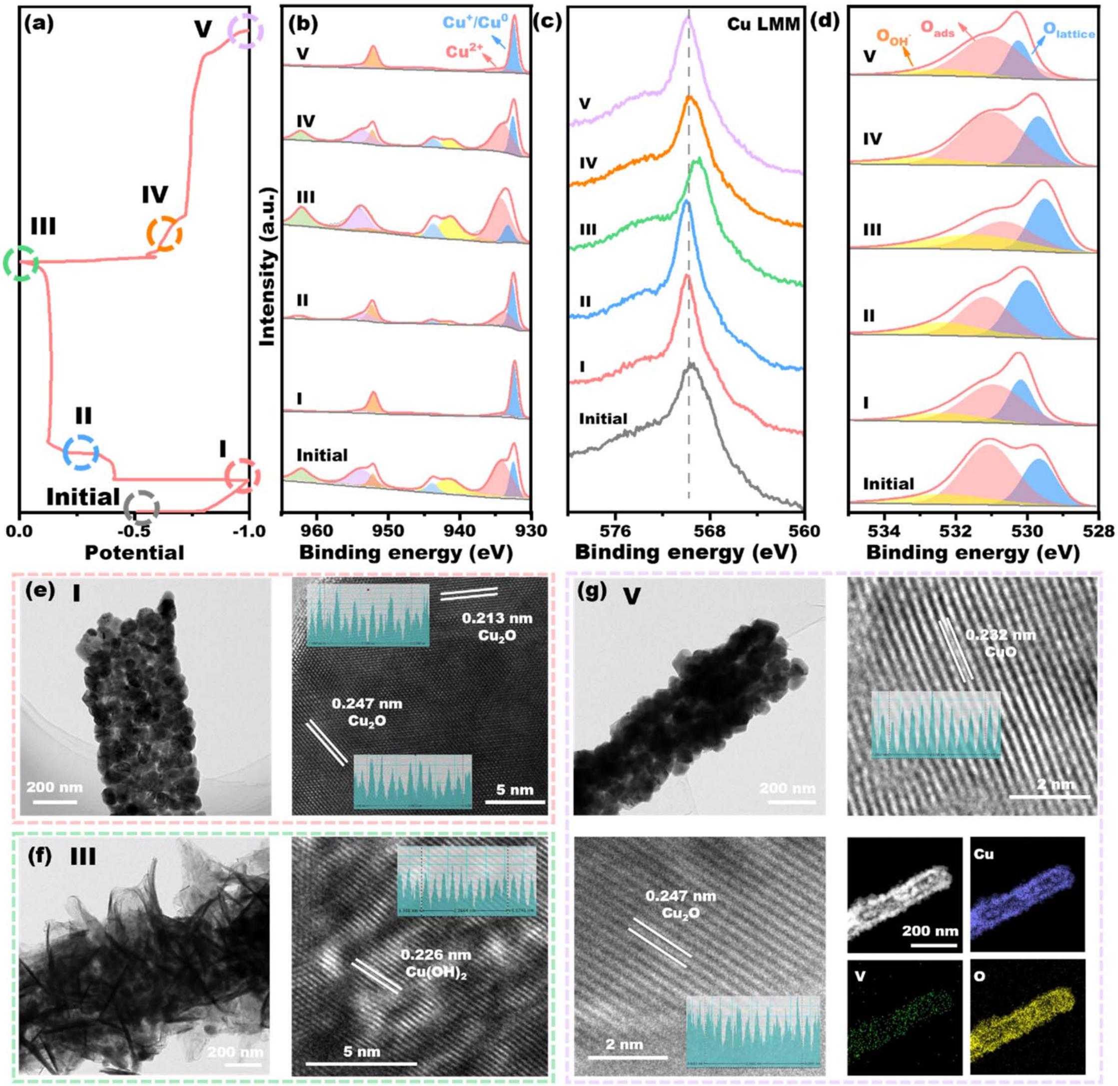

Fig. 5 *Ex situ* measurements to investigate the V-Cu$_x$O electrode during charge and discharge processes. (a) GCD curves. (b) Cu 2p, (c) Cu LMM and (d) O 1s XPS spectra. HRTEM images (e–g) of the V-Cu$_x$O electrode at states I, III and V during charge and discharge processes.

leading to greater ion accessibility and transport compared to the Cu$_x$O electrode.

The GCD curves in Fig. 4d also indicate that V-Cu$_x$O has higher areal capacity at a current density of 50 mA cm^{-2} than Cu$_x$O. The measured high active areal mass loadings of the self-supporting V-Cu$_x$O and Cu$_x$O electrodes are ~12.80 and 20.08 mg cm^{-2}, indicating that this preparation method can efficiently transform inactive copper into active material for energy storage. The GCD curves of V-Cu$_x$O (Fig. 4e) and Cu$_x$O (Fig. S14b†) electrodes at various current densities exhibit several plateaus during charging and discharging, indicating that faradaic reactions occur and can contribute to the energy storage capacity. At a current density of 50 mA cm^{-2}, the areal capacities of the V-Cu$_x$O and Cu$_x$O electrodes reach 31.65 and 20.39 mAh cm^{-2}, respectively. However, the capacity retention (Fig. 4f) of Cu$_x$O at 100 mA cm^{-2} is 29.4%, much lower than that of V-Cu$_x$O (71.1%). This improvement can be attributed to V doping, which leads to more efficient ion transfer and thus further improves the rate capability.

To investigate the contributions of diffusion-controlled faradaic reactions and surface-controlled capacitive processes during charge/discharge, the following relationships were used to analyze the CV curves:[41–43]

$$i = av^b \tag{6}$$

$$\log i = b \log v + \log a \tag{7}$$

$$i = k_1 v + k_2 v^{1/2} \tag{8}$$

$$\frac{i}{v^{1/2}} = k_1 v^{1/2} + k_2 \tag{9}$$

where i and v are the peak current and scan rate, a and b are constants, and $k_1 v$ and $k_2 v^{1/2}$ represent the surface-controlled capacitive process and diffusion-controlled process,

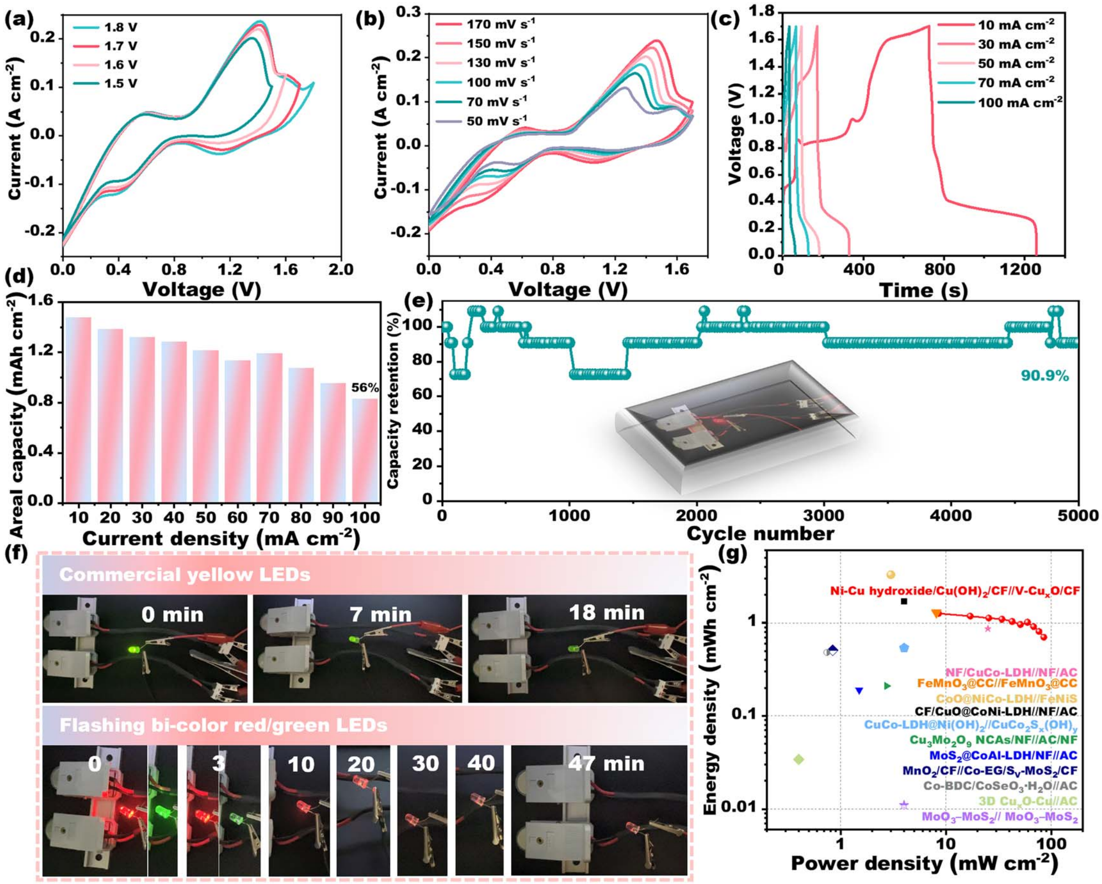

Fig. 6 Data exploring the performance of the Ni–Cu hydroxide/$Cu(OH)_2$/CF//V-Cu_xO/CF AEESD. (a) CV curves in different voltage ranges. CV curves (b) and GCD curves (c) of the device at different scan rates and current densities, respectively. (d) The rate performance of the devices. (e) Cycling performance (inset: a photograph of a LED light (2 V) charged by two devices in series). (f) Digital photographs of two devices in series used to power commercial yellow and flashing bi-color red/green LEDs. (g) Ragone plot comparing the performance of this work with other state-of-art devices.

respectively.[44,45] By determining the relationship between *i* and *v*, the *b*-value can be obtained as shown in Fig. 4g. *b* is 0.55, indicating that the V-Cu_xO electrode is mainly governed by the diffusion-controlled process, similar to previous reports.[40,41] Fig. 4h shows that the capacitive contribution of the V-Cu_xO electrode increases from 26% to 80% at 30 and 150 mV s^{-1}, respectively. The percentage of diffusion and capacitive contributions for the Cu_xO electrode is provided in Fig. S15.†

The Nyquist plots in Fig. 4i and the corresponding fitting results (Fig. S16†) show that the charge transfer resistance (R_{ct}) of V-Cu_xO (0.67 Ω) is significantly lower than that of Cu_xO (1.19 Ω), consistent with V doping decreasing the resistance during charge transfer. The V-Cu_xO electrode exhibits high-capacity retention upon cycling (Fig. 4j), maintaining 95% of the initial value after 5000 cycles. The areal capacity of the V-Cu_xO electrode is superior to that of most electrode materials reported in the literature, for example, $CuCo_2S_x(OH)_y$ (2.94 F cm^{-2} at 5 mA cm^{-2}),[46] Co–Fe–O-NPs@MXene (0.949 mAh cm^{-2} at 1 mA cm^{-2}),[47] 4D-printed $Ti_3C_2T_x$ hydrogel electrode (3.32 F cm^{-2} at 10 mV s^{-1}),[48] and other electrodes materials provided in Table S6†.

Mechanistic investigation

Based on the GCD curve in Fig. 5a, several selected states (I to V) during charge/discharge were analyzed through *ex situ* XPS and HRTEM, to investigate the energy storage mechanism of V-Cu_xO. Fig. 5b exhibits the *ex situ* Cu 2p XPS spectra. The Cu^{2+} and $Cu^{+/0}$ peaks change from state I to V: the peak area ratio of $Cu^{2+}/Cu^{+/0}$ (Table S7†) increases from state I to III and then decreases. From state I to III in the discharge process, more Cu^{2+} ions are generated, which is consistent with the Cu LMM XPS spectra (Fig. 5c) exhibiting a shift to lower binding energy. The reverse trend can be observed during the charging process. These results indicate that the conversion between Cu^{2+} and $Cu^{+/0}$ is utilized to store energy when the electrode is in contact with the KOH electrolyte. In addition, the $O_{lattice}$ and O_{OH}^- peaks in Fig. 5d exhibit clear changes. The HRTEM results (Fig. 5e–g) demonstrate that lattice fringes belonging to $Cu(OH)_2$ can be measured in state III but not in state I and V, indicating that the charge transfer occurred between V-Cu_xO and the KOH electrolyte. Considering the peak area ratio of $O_{OH}^-/O_{lattice}$ (Table S8†), there is an increase in the ratio moving from state I to III, also indicating the gradual formation of

$Cu(OH)_2$. This ratio then declines again from state III to V. Element mapping results (Fig. 5g) confirm that V remains in the electrode throughout the process.

Electrochemical performance

For exploring practical applications, we constructed an AEESD. The device was assembled using V-Cu_xO/CF and Ni–Cu hydroxide/$Cu(OH)_2$/CF as the negative and positive electrodes, with KOH electrolyte. The CV curves with different voltage windows of the devices at a scan rate of 100 mV s^{-1} are shown in Fig. 6a. After considering the polarization and safety requirements, we selected a voltage window of 0–1.7 V. The CV curves of the device at different scan rates are exhibited in Fig. 6b, and no clear distortion can be observed with an increase in the scan rate, indicating the AEESD's desirable reversibility and rate capability. GCD curves of the device at different current densities (Fig. 6c) exhibit typical battery-type behavior, with voltage plateaus during charge/discharge processes. The device can provide a specific areal capacity of 1.48 mAh cm^{-2} at 10 mA cm^{-2}. The rate capability (Fig. 6d) of the device was calculated from GCD curves and was found to be 56% of the initial capacity at 100 mA cm^{-2}.

As shown in Fig. 6e, the device can maintain good capacity retention (90.9% after 5000 cycles). Digital photographs showing LED lights charged by two AEESDs in series are given in Fig. 6f, indicating stable discharge performance. The two devices can power commercial yellow and flashing red/green LEDs for up to 18 and 47 min respectively. The constructed device can deliver an energy density of 1.26 mWh cm^{-2} with a power density of 8.50 mW cm^{-2} at 10 mA cm^{-2}, and still retain 0.71 mWh cm^{-2} with a power density of 85 mW cm^{-2} at 10 mA cm^{-2}. As shown in Fig. 6g, the performance of the constructed device is better than that of some previously reported AEESD systems, such as CuCo-LDH@$Ni(OH)_2$//$CuCo_2S_x(OH)_y$ (0.54 mWh cm^{-2} at 4.01 mW cm^{-2}),[46] CF/CuO@CoNi-LDH//NF/AC (1.7 mWh cm^{-2} at 4 mW cm^{-2}),[49] NF/CuCo-LDH//NF/AC (0.87 mWh cm^{-2} at 25 mW cm^{-2}),[50] and other devices as provided in Table S9.†

Conclusions

In this work, we report a self-supporting V-doped Cu_xO system as a negative electrode for AEESDs. This was achieved *via in situ* transformation of a nanorod array precursor along with V doping. Theoretical and experimental analyses determined that the vanadium introduced within the lattice can successfully modulate the electronic structure of the materials through partial isomorphic substitution at copper sites. The porous structure formed through *in situ* chemical oxidation endows the material with highly-exposed active sites. Moreover, the narrow band gap, oxygen vacancies, and strong interfacial electronic interactions in V-Cu_xO can drive electron transfer, thereby enhancing its electrical conductivity and reaction kinetics for energy storage. Consequently, the V-Cu_xO electrode material shows strong electrochemical performance, with an outstanding specific areal capacity of 31.65 mAh cm^{-2} at 50 mA cm^{-2}, together with 71.1% retention at 100 mA cm^{-2}. Moreover, an AEESD constructed using V-Cu_xO achieves a high energy density of 1.26 mWh cm^{-2} at a power density of 8.50 mW cm^{-2} and retains 0.71 mWh cm^{-2} at a power density of 85 mW cm^{-2}. The AEESD exhibits desirable discharge performance and can power LED lighting for a prolonged period of time. This work provides novel insights into how the crystal structure of copper-based oxides can be employed to enhance the electrochemical performance.

Data availability

The data supporting this article have been included as part of the ESI.†

Author contributions

Jiaxin Luo: conceptualization, methodology, software, investigation, formal analysis, writing – original draft. Yang Qin: methodology, writing – review & editing. Meina Tan: investigation. Shengtong Lv: investigation. Fazhi Zhang: supervision, conceptualization. Xuhui Zhao: supervision, conceptualization. Yiping Wang: supervision, conceptualization. Gareth R. Williams: supervision, conceptualization, writing – review & editing. Xiaodong Lei: supervision, resources, conceptualization, writing – review & editing.

Conflicts of interest

The authors confirm no conflicts of interest.

Acknowledgements

We acknowledge the National Natural Science Foundation of China (no. 22278020 and 2177060378), the Program for Changjiang Scholars, Innovative Research Teams in Universities (no. IRT1205), and the Fundamental Research Funds for Central Universities (no. 12060093063 and XK1803-05).

References

1 B. Dunn, H. Kamath and J. Tarascon, *Science*, 2011, **334**, 928–935.
2 P. Brockway, A. Owen, L. Brand-Correa and L. Hardt, *Nat. Energy*, 2019, **4**, 612–621.
3 M. Zhou, P. Bai, X. Ji, J. Yang, C. Wang and Y. Xu, *Adv. Mater.*, 2021, **33**, 2003741.
4 J. Song, H. Fan, Y. Wang, Q. Li, J. Zhao, C. Shao, T. Li, Y. Jin, S. Liu and W. Liu, *Small*, 2024, **20**, 2309097.
5 J. Guo, B. He, W. Gong, S. Xu, P. Xue, C. Li, Y. Sun, C. Wang, L. Wei, Q. Zhang and Q. Li, *Adv. Mater.*, 2024, **36**, 2303906.
6 Y. Zhang, H. Mei, Y. Cao, X. Yan, J. Yan, H. Gao, H. Luo, S. Wang, X. Jia, L. Kachalova, J. Yang, S. Xue, C. Zhou, L. Wang and Y.-h. Gui, *Coord. Chem. Rev.*, 2021, **438**, 213910.
7 M. Feng, Y. Zhang, X. Zhu, W. Chen, W. Lu and G. Wu, *Angew. Chem., Int. Ed.*, 2023, **62**, e202307195.

8 S. Sahoo, K. Krishnamoorthy, P. Pazhamalai and S. Kim, *Nanoscale*, 2018, **10**, 13883–13888.

9 V. Nithya and N. Arul, *J. Power Sources*, 2016, **327**, 297–318.

10 S. Chen, H. Jiang, Q. Cheng, G. Wang, S. Petr and C. Li, *Chem. Eng. J.*, 2021, **403**, 126380.

11 H. Xu, H. Dong, X. Liu, H. Qiao, G. Chen, F. Du, Y. Dall'Agnese and Y. Gao, *ACS Appl. Mater. Interfaces*, 2023, **15**, 53549–53557.

12 Q. Wu, S. Zhao, L. Yu, X. Zheng, Y. Wang, L. Yu, C. Nan and G. Cao, *J. Mater. Chem. A*, 2019, **7**, 13205–13214.

13 J. Luo, Y. Qin, D. Zhang, T. Dou, M. Tan, F. Zhang, X. Zhao, Y. Wang, L. Zheng and X. Lei, *Chem. Eng. J.*, 2024, **485**, 149945.

14 L. Xu, W. Zhou, S. Chao, Y. Liang, X. Zhao, C. Liu and J. Xu, *Adv. Energy Mater.*, 2022, **12**, 2200101.

15 R. Madhu, A. Karmakar, S. Kumaravel, S. Sankar, K. Bera, S. Nagappan, H. Dhandapani and S. Kundu, *ACS Appl. Mater. Interfaces*, 2022, **14**, 1077–1091.

16 H. Dong, T. Yao, X. Ji, Q. Zhang, X. Lin, B. Zhang, C. Ma, L. Meng, Y. Chen and H. Wang, *ACS Appl. Mater. Interfaces*, 2024, **16**, 22055–22065.

17 Y. Guan, S. Zhou, L. Tan, R. Zhao, Q. Zhang, H. Zhu, X. Li, Z. Dong, H. Duan, D. Li, V. Nicolosi, Y. Cong and K. Li, *Energy Storage Mater.*, 2025, **75**, 104032.

18 L. Kang, S. Liu, Q. Zhang, J. Zou, J. Ai, D. Qiao, W. Zhong, Y. Liu, S. C. Jun, Y. Yamauchi and J. Zhang, *ACS Nano*, 2024, **18**, 2149–2161.

19 P. Zhou, X. Lv, D. Xing, F. Ma, Y. Liu, Z. Wang, P. Wang, Z. Zheng, Y. Dai and B. Huang, *Appl. Catal., B*, 2020, **263**, 118330.

20 G. Qu, J. Wang, G. Liu, B. Tian, C. Su, Z. Chen, J. Rueff and Z. Wang, *Adv. Funct. Mater.*, 2019, **29**, 1805227.

21 L. Jin, X. Liu, Z. Wang, J. Luo, L. Zheng, M. Zhang and Y. Ao, *ACS Appl. Mater. Interfaces*, 2023, **15**, 58517–58528.

22 Z. Lu, J. Cheng, L. Zhang, Q. Yang, H. Pan, D. Wu, Y. Gao, X. Huang, T. Wang and X. Chen, *J. Alloys Compd.*, 2021, **856**, 158075.

23 D. Zhang, Y. Shao, X. Kong, M. Jiang, D. Lei and X. Lei, *Electrochim. Acta*, 2016, **218**, 294–302.

24 W. Sun, P. Wang, Y. Jiang, Z. Jiang, R. Long, Z. Chen, P. Song, T. Sheng, Z. Wu and Y. Xiong, *Adv. Mater.*, 2022, **34**, 2207691.

25 D. Yang, L. Cao, L. Feng, J. Huang, K. Kajiyoshi, Y. Feng, Q. Liu, W. Li, L. Feng and G. Hai, *Appl. Catal., B*, 2019, **257**, 117911.

26 M. Zhao, C. Guo, L. Gao, X. Kuang, H. Yang, X. Ma, C. Liu, X. Liu, X. Sun and Q. Wei, *Inorg. Chem. Front.*, 2021, **8**, 3266–3272.

27 Z. Gu, N. Yang, P. Han, M. Kuang, B. Mei, Z. Jiang, J. Zhong, L. Li and G. Zheng, *Small Methods*, 2019, **3**, 1800449.

28 Y. Tao, J. Yuan, X. Qian, Q. Meng, J. Zhu, G. He and H. Chen, *Inorg. Chem. Front.*, 2021, **8**, 2271–2279.

29 Z. Li, D. Zhao, C. Xu, J. Ning, Y. Zhong, Z. Zhang, Y. Wang and Y. Hu, *Electrochim. Acta*, 2018, **278**, 33–41.

30 P. Cui, P. Zhang, X. Chen, X. Chen, T. Wan, Y. Zhou, M. Su, Y. Liu, H. Xu and D. Chu, *ACS Appl. Mater. Interfaces*, 2023, **15**, 43745–43755.

31 J. Yang, X. Xiao, P. Chen, K. Zhu, K. Cheng, K. Ye, G. Wang, D. Cao and J. Yan, *Nano Energy*, 2019, **58**, 455–465.

32 H. Qin, Y. Ye, J. Li, W. Jia, S. Zheng, X. Cao, G. Lin and L. Jiao, *Adv. Funct. Mater.*, 2023, **33**, 2209698.

33 H. Chavan, C. Lee, A. Inamdar, J. Han, S. Park, S. Cho, N. Shreshta, S. Lee, B. Hou, H. Im and H. Kim, *ACS Catal.*, 2022, **12**, 3821–3831.

34 A. Vali, H. Jee, N. Myung and K. Rajeshwar, *ChemElectroChem*, 2021, **8**, 1251–1258.

35 A. Yamuna, T. Chen, S. Chen and T. Jiang, *Microchim. Acta*, 2021, **188**, 277.

36 H. Tian, Z. Zhang, H. Fang, H. Jiao, T. Gao, J. Yang, L. Bian and Z. Wang, *Appl. Catal. B Environ. Energy*, 2024, **351**, 124001.

37 D. Zhang, X. Yuan, Y. Xin, T. Liu, H. Han, G. Du and A. Teng, *Acta Chim. Sin.*, 2024, **82**, 274–280.

38 Y. Li, F. Zhang, W. Gao and Z. Zhan, *Ionics*, 2021, **27**, 2335–2344.

39 K. Ranjith, C. Dong, Y. Lu, Y. Huang, C. Chen, P. Saravanan, K. Asokan and R. Rajendra Kumar, *ACS Sustain. Chem. Eng.*, 2018, **6**, 8536–8546.

40 D. Zhang, X. Kong, F. Zhang and X. Lei, *Adv. Electron. Mater.*, 2020, **6**, 1900953.

41 S. Pervez and M. Iqbal, *Small*, 2023, **19**, 2305059.

42 K. Li, X. Wang, X. Wang, M. Liang, V. Nicolosi, Y. Xu and Y. Gogotsi, *Nano Energy*, 2020, **75**, 104971.

43 K. Li, X. Wang, S. Li, P. Urbankowski, J. Li, Y. Xu and Y. Gogotsi, *Small*, 2020, **16**, 1906851.

44 Q. Chen, Z. Tang, H. Li, W. Liang, Y. Zeng, J. Zhang, G. Hou and Y. Tang, *ACS Appl. Mater. Interfaces*, 2024, **16**, 18824–18832.

45 S. Chen, H. Zhang, X. Li, Y. Liu, M. Zhang, X. Gao, X. Chang, X. Pu and C. He, *Dalton Trans.*, 2023, **52**, 4826–4834.

46 F. Lu, Y. Ji, D. Shi, J. Yao, P. Zhang and S. Zhang, *Inorg. Chem. Front.*, 2023, **10**, 6369–6383.

47 A. Alam, G. Saeed, K. Kim and S. Lim, *J. Energy Storage*, 2022, **55**, 105592.

48 K. Li, J. Zhao, A. Zhussupbekova, C. Shuck, L. Hughes, Y. Dong, S. Barwich, S. Vaesen, I. Shvets, M. Möbius, W. Schmitt, Y. Gogotsi and V. Nicolosi, *Nat. Commun.*, 2022, **13**, 6884.

49 Q. Wu, F. Li, H. Sheng, Y. Qi, J. Yuan, H. Bi, W. Li, E. Xie and W. Lan, *ACS Appl. Mater. Interfaces*, 2024, **16**, 23241–23252.

50 S. Mane, A. Teli, H. Yang, E. Kwon, N. Nimbalkar, D. Patil and J. Shin, *J. Energy Storage*, 2023, **62**, 106941.